Heliyon 9 (2023) e21633

Contents lists available at ScienceDirect

Heliyon

journal homepage: www.cell.com/heliyon

Influence of Zn-substitution on structural, magnetic, dielectric, and electric properties of Li–Ni–Cu ferrites

Jannatul Ferdaus [a], Mithun Kumar Das [a,*], Anamika Dey [a], Bablu Chandra Das [b], F. Alam [b], Mashudur Rahaman [c], Md Azizul Hoque [c], Muhammad Shahriar Bashar [c]

[a] Department of Physics, Comilla University, Cumilla, 3506, Bangladesh
[b] Department of Physical Sciences, Independent University, Bangladesh
[c] Institute of Fuel Research and Development (IFRD), Bangladesh Council of Scientific and Industrial Research (BCSIR), Dhaka, 1205, Bangladesh

ARTICLE INFO

Keywords:
Magnetization
Permeability
Dielectric
Impedance
Electric modulus

ABSTRACT

The polycrystalline $Li_{0.15}Ni_{0.6-x}Zn_xCu_{0.1}Fe_{2.15}O_4$ ferrites are fabricated by the method of conventional solid-state reaction technique. The X-ray diffraction (XRD) confirms that the structure of the composition is a single-phase cubic spinel structure for all samples. The particle size of the compositions is varied from 36 to 52 nm. The lattice parameter and densities are found to increase with enhancing *Zn* content, as the ionic radius and atomic weight of Zn are greater than Ni. The porosity exhibits a decreasing trend. The average grain size determined using Field Emission Scanning Microscopy (FESEM) increases until $x = 0.40$, then declines. The Energy-Dispersive Spectroscopy (EDS) examination revealed that the percentage of obtained elements is well matched with the stoichiometric elements. The addition of Zn content acts as an accelerator for enhancing the value of the real part of initial permeability and the highest value is obtained ($\mu_i' = 276$) for the $x = 0.40$ sample, as well as the highest relative quality factor (RQF) of around 3000. The loss factor for the Zn substituted composition is nine times lower than for the parent composition. The optimum saturation magnetization of around 77.49 emu/g is found for the $x = 0.40$ sample. The maximum dielectric constant ($\varepsilon' = 2.85 \times 10^3$) is found for $x = 0.10$ samples at 10 kHz. Further, from impedance studies, the non-Debye type dielectric relaxation is seen for the Zn-substituted samples. The observed region of the imaginary electric modulus peak signifies the transition of charge carrier mobility from a larger range to a short-range distance. The phenomenon of ac conductivity is attributed to the process of the small polaron hopping mechanism.

1. Introduction

Ferrimagnetic oxides or ferrites have become a practical magnetic material and have risen to an important place in many branches of electrical engineering over the last two or three decades. Their high degree of compositional diversity and good magnetic performance make them a popular choice in research. Most electrical conduction in ferrites occurs by hopping electrons among ions of the same element in numerous valence states and randomly scattered over comparable crystallographic lattice sites [1–3]. The crystal structure of spinel ferrite is characterized by the presence of A-sites (tetrahedral) and B-sites (octahedral), as specified by the chemical formula AB_2O_4. The magnetic and dielectric properties depend on ion distribution on tetrahedral and octahedral sites. Additionally, it

* Corresponding author. Department of Physics, Comilla University, Cumilla, Bangladesh.
E-mail addresses: mkdas@cou.ac.bd, mkdas.ju@gmail.com (M.K. Das).

https://doi.org/10.1016/j.heliyon.2023.e21633
Received 16 June 2023; Received in revised form 7 October 2023; Accepted 25 October 2023
Available online 26 October 2023

is thought that Zn ions change the Curie temperature, lattice parameter, and saturation magnetization [4]. It is well recognized that the inclusion of Cu in the Ni–Zn ferrite composition has a notable impact on reducing the sintering temperature (T_s). The main obstacles faced by high-performance Ni–Zn ferrites are expanding the frequency range of applicability and reducing energy consumption. Several attempts have been undertaken to enhance the electrical resistivity, dielectric, and magnetic characteristics of mixed Ni–Zn ferrites. Many scientists now accept that substituting one material for another is the most effective technique for modifying its morphological, electrical, and magnetic characteristics [5–11]. Whereas, the interest in research in Ni–Cu–Zn is exaggerated day by day, since it has vast applications in multilayer chip inductors, multilayer LC filters, magnetic temperature sensors, and humidity sensors [12–16]. In addition, Ni–Zn–Cu ferrites exhibit lower densification temperatures than Ni–Zn ferrites and superior characteristics at higher frequencies compared to Mn–Zn ferrites [17,18]. Moreover, several studies have focused on Ni–Cu–Zn spinel ferrites due to the excellent electrical and magnetic characteristics shown by ferrites containing copper. The Jahn-Teller effect causes Cu-ferrite to undergo a structural phase as well as a decrease in crystal symmetry to tetrahedral, distinguishing it from other spinel ferrites [19]. Li-ferrites have excellent relaxation and anisotropic characteristics in comparison to other ferrites due to distinct substitutions [20,21]. Li-based ferrite is a versatile magnetic material that finds extensive use in both low- and high-frequency devices, making it very useful for many daily uses [22]. However, in this study, Zn^{2+} was chosen as a substituted ion to improve the composition's densification and electromagnetic properties. The addition of Zn was seen to enhance the electromagnetic characteristics, including the initial permeability, saturation magnetization, and impedance [23,24]. The previous investigation showed that the inclusion of Zn content significantly contributes to the enhancement of density, magnetic moment, and, average grain size [25,26]. The addition of the Jahn-Teller ion Zn^{2+} to the $LiNiFe_2O_4$ ferrite resulted in a significant increase in the magnetostriction coefficient, hence improving the electromagnetic characteristics of the material [27]. Therefore, this research is being carried out for Zn doping Li–Ni–Cu ferrite to understand the changing behavior of the investigated samples and to optimize them for different applications. Here, we have thoroughly examined the impact of Zn substitution on the structural, morphological, magnetic, and electrical properties of Li–Ni–Cu ferrites.

2. Experimental procedure

2.1. Synthesis

Compositions of $Li_{0.15}Ni_{0.6-x}Zn_xCu_{0.1}Fe_{2.15}O_4$ (LNZCFO) (where x = 0.00–0.50; in steps of 0.10) were prepared by using the traditional solid-state reaction method [28]. According to stoichiometric proportion, highly pure raw materials of Li_2CO_3 (99.0 %, CAS No. 554-13-2, Sigma-Aldrich), NiO (99.9 %, CAS No. 1313-99-1, Sigma-Aldrich), ZnO (99.9 %, CAS No. 1314-13-2, Sigma-Aldrich), CuO (99.99 %, CAS No. 1317-38-0, Sigma-Aldrich), and Fe_2O_3 (99.9 %, CAS No. 1309-37-1, Thermo Scientific Chemicals) were weighed. The hand-milling process was carried out by using an agate mortar in an acetone medium to form a homogeneous mixture. The combined powders were then calcined at 800 °C for 5 h. The further grinding of the calcined powders results in enhanced homogeneity of the sample. A binder consisting of 10 % polyvinyl alcohol (PVA) was incorporated into the ground powder. Subsequently, a pressure of 5 tons per square centimeter was used to shape the samples into disks and pellets. The samples were sintered in air for 5 h at 1200 °C, and ready for characterization.

2.2. Characterization

The structural characterization of ferrites was conducted using an advanced X-ray diffractometer with CuK_α as a target ($\lambda = 1.5418$ Å). The lattice parameter for each peak of the cubic spinel ferrites was calculated by using the formula $a_0 = d\sqrt{h^2 + k^2 + l^2}$, where (h k l) is the miller indices, a_0 is the lattice parameter and d is the inter-planer distance obtained by the equation $2d_{hkl}sin\theta = n\lambda$. The FESEM was used to analyze the microstructures of ferrites. The bulk density(ρ_B), and the theoretical density (ρ_{th}) were determined using the following expression: $\rho_B = \frac{M}{\pi r^2 t}$, and $\rho_{th} = \frac{8M_A}{N_A a_0^3}$, where M is the sample mass, r the radius, t the pellet thickness, M_A the molecular weight, and N_A Avogadro's number. The calculation of porosity (P) as a percentage was performed using the equation: $P = \frac{\rho_B}{\rho_{th}} \times$ 100%. The investigation of frequency-dependent dielectric and magnetic characteristics was conducted using a Wayne Kerr Impedance Analyzer (Model no. 6500B). The real part of initial permeability (μ_i') is calculated with the following relation: $\mu_i' = \frac{L_s}{L_0}$, where, L_s is the winding coil's self-inductance with a sample, L_0 ($= \frac{\mu_0 N^2 S}{\pi d}$) [29] is its inductance without the sample core, N is the number of turns of the coil (n = 4), S is the area of the cross-section and $\overline{d}$ is the mean diameter. The formula used to determine the RQF is $RQF = \frac{\mu_i'}{tan\ \delta_M}$ [30]. A Vibrating Sample Magnetometer (VSM) was used to measure the magnetization of various samples. The dielectric constant (ε') was found from the relations: $\varepsilon' = \frac{C}{C_0}$, where, C_o is the capacitance of vacuum or free space, and C reveals the capacitance with the dielectric medium. The electrical properties were carried out on disk-shaped specimens in the high-frequency regime. The ac conductivity was calculated with the following equation (σ_{ac}): $\sigma_{ac} = \omega\varepsilon_0\varepsilon' tan\delta_E$, where ε_0 represents free space permittivity, ω represents angular frequency, and $tan\delta_E$ represents dielectric loss [31,32].

3. Results and discussion

3.1. Structural analysis

The XRD patterns of variously studied ferrites are shown in Fig. 1. Sharp and clearly defined peaks are seen in the XRD pattern with the Miller indices (220), (311), (222), (400), (422), (511) and (440), which confirms the single phase cubic spinel structure. All of the peaks in the pattern also match well with the characteristic reflections that have been previously reported [27]. The leftward shift of peaks seen with the increase in Zn concentration suggests an increase in the a_0. The Scherrer formula is used to evaluate the average particle size (D) through the FWHM of the diffraction peaks for each sample [33]. The D is predicted to range from 36 to 52 nm, as shown in Table 1. Fig. 2 depicts the a_0 for different LNZCFO ferrites. The extrapolation of the fitted lines to the y-axis yields an estimate of the precise a_0. It is evident that the lattice parameter a_0 exhibits an upward trend as the concentration of Zn increases, following Vegard's law [34]. It has been observed that the value of a_0 ranges from 8.38164 Å to 8.39343 Å. There are two notable factors contributing to the observed rise in a_0: (i) the ionic radius of Zn(0.750 Å) is observed to be larger than that of Ni(0.690 Å), leading to an increase in the a_0 upon the addition of Zn content, (ii) this increase in a_0 can be attributed to the volume differences between the constituent cations, where the substitution of Ni^{2+}(0.078 nm) with Zn^{2+}(0.083 nm), a larger ion, causes the unit cell to expand [35]. In the context of doping, the substitution of Ni^{2+} ions with Zn^{2+} ions inside the NiO lattice results in lattice distortion. This distortion arises from the disparities in ionic radius and ionic charge between the two ions. Consequently, an increased number of oxygen vacancies are generated to maintain charge equilibrium. The lattice distortion also impacts the structural characteristics of the NiO structures. The result indicates that when the concentration of Zn in Ni-ferrites rises, there is a reduction in lattice strain and an increase in lattice constant [36,37]. The findings of this research demonstrate that the absence of Zn in the composition results in a decrease in the lattice constant, mostly owing to an increase in lattice strain. However the lattice constant exhibits an increase as the Zn concentration rises, mostly attributed to the reduction in lattice strain. The obtained result is in good agreement with the earlier reported result [36,37]. The values of a_0 for different compositions investigated are shown in Table 1.

3.2. Surface morphology and EDS analysis

The surface morphology and elemental analysis were conducted using an FESEM equipped with an EDS system. Figs. 3 and 4 show the FESEM micrographs and EDS analyses, respectively. The average grain size ($\overline{D}$) is determined from a grain distribution histogram using ImageJ software. The magnitude of the $\overline{D}$ falls between the range of 4–6 μm. Anomalous grain development provides a substantial activation energy for the movement of grain boundaries. Analysis of FESEM images reveals ferromagnetic properties are associated with significantly larger grains. Certain small pores are observable, with some being entrapped within the ferrite structure due to diffusion delays occurring during the sintering process. However, it can be seen that the sintered structures exhibit greater strength in comparison to the non-sintered samples, mostly attributed to their lower presence of defects and pores [38]. The obtained values are presented in Table 1.

The EDS spectra obtained using FESEM provide valuable information on the effective atomic concentration of various constituents present in the top surface layers of the materials under investigation [39]. The EDS investigation demonstrated that the mass percentages of the elements found closely correspond to the stoichiometric elements, except for oxygen. The formation of oxygen vacancies may occur at elevated temperatures during the sintering process. The values are presented by the tables in the inset of Fig. 4. For the $x = 0.30$ sample, the element mapping was carried out by EDS spectra. Fig. 5 revealed that the element mapping confirms the presence of O, Fe, Ni, Cu, and Zn in the investigated sample which is homogeneously distributed.

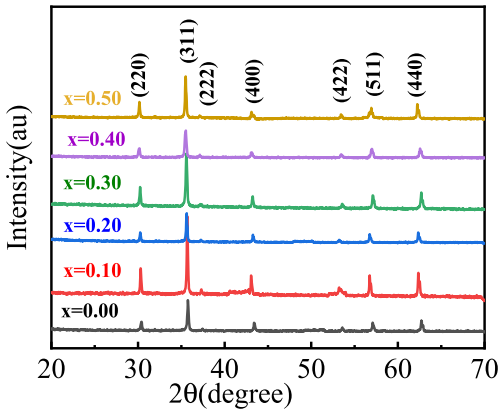

Fig. 1. The XRD patterns for various $Li_{0.15}Ni_{0.6-x}Zn_xCu_{0.1}Fe_{2.15}O_4$ ferrites.

Table 1
The a_0, D, $\overline{D}$, ρ_{th}, ρ_B, and P for various $Li_{0.15}Ni_{0.6-x}Zn_xCu_{0.1}Fe_{2.15}O_4$ ferrites.

Content, x	a_0 (Å)	D (nm)	$\overline{D}$ (μm)	ρ_{th} (g/cm^3)	ρ_B (g/cm^3)	(P%)
0.00	8.3816	52	4.01	5.11	4.32	15
0.10	8.3824	51	4.45	5.13	4.39	14
0.20	8.3828	49	5.09	5.14	4.42	14
0.30	8.3830	43	5.68	5.15	4.53	12
0.40	8.3840	36	6.04	5.17	4.76	7
0.50	8.3934	47	3.89	5.16	4.74	8

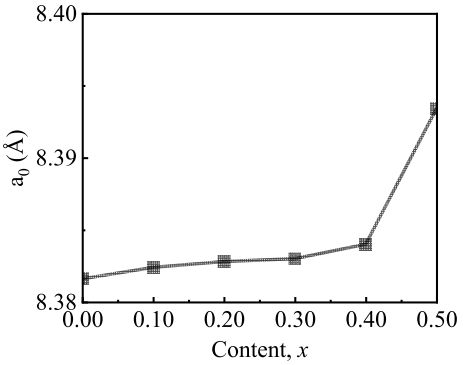

Fig. 2. Variation of a_0 with Zn content for various $Li_{0.15}Ni_{0.6-x}Zn_xCu_{0.1}Fe_{2.15}O_4$ ferrites.

3.3. Density and porosity

The electric and magnetic characteristics of ferrite compounds are notably influenced by their density, along with several other factors. Molecular weight, a_0, and other factors are used to compute ρ_{th}. Materials that possess a high density have little porosity and demonstrate favorable electric and magnetic properties. Fig. 6 demonstrates the effect of introducing Zn on the rise of both the ρ_{th} and the ρ_B. The atomic weight of the constituent elements is responsible for these phenomena. The substituent Zn has a larger atomic weight (65.38 amu) than the Ni atom (58.69 amu). As a result, there is an expected rise in the variable ρ_B. Fig. 6 further demonstrates that the value of ρ_{th} is greater than ρ_B, indicating that during the sintering process, the samples may have tiny fractures, holes, and atomic vacancies inside the lattice structure [40]. The aforementioned imperfections are taken into consideration while determining the ρ_B of the bulk samples. In contrast, the value of ρ_{th} is determined by the use of the lattice constant and the volume of the unit cell, which is not influenced by the presence of any defects. The P of the compositions, on the other hand, demonstrates the opposite trend. The addition of Zn causes disappears of voids and holes making the composition denser with a smaller P. Two types of porosity contribute to the P value of ceramic samples: intragranular and intergranular [41]. As a result, the formula for the total porosity is $P=P_{intra}+P_{inter}$. The average grain size is the key factor influencing intergranular porosity. The measured values are shown in Table 1.

3.4. Real part of initial permeability

The parameter μ_i' provides insights into the dynamic magnetic characteristics of materials and their efficacy in high-frequency applications. In Fig. 7, the frequency dependence of μ_i' for different LNZCFO materials is shown to range from 10 kHz to 100 MHz. The data shows that the value of μ_i' exhibits a rising pattern as the concentration of Zn increases. It reaches its peak value ($\mu_i'=276$) for $x=0.40$ composition, which is more than nine times higher than the value observed for the parent composition ($\mu_i'=30$). It has been found that the value of μ_i' stays merely constant up to a certain frequency referred to as the resonance frequency. Subsequently, it exhibits a decreasing pattern with a rising frequency. This decrease of μ_i' is due to intragranular pores and higher-frequency impurities on the sample surface that result in a pinning effect. This effect hinders the mobility of domain walls and the rotation of spins, hence reducing their influence on the parameter μ_i'. According to Snoek's law ($f_r\mu_i'=$ constant), the μ_i' and resonance frequency (f_r) are inversely proportional [42,43]. No resonance peak is seen for the $x=0.00$ sample, which may be because f_r is beyond the measurable frequency range (more than 100 MHz). Evidence suggests that polycrystalline ferrite permeability is affected by two magnetizing mechanisms: spin rotation and domain wall motion [44,45].

3.5. Relative quality and loss factor

Fig. 8 displays the RQF vs. frequency representation for all compositions, revealing an expected trend of rising values as the Zn content rises. The RQF is used as a performance metric for materials in many device applications. As the frequency increases, there is a rise in the RQF. However, a subsequent decline is seen after a certain frequency value reaches its peak. The sample with $x=0.40$ has a

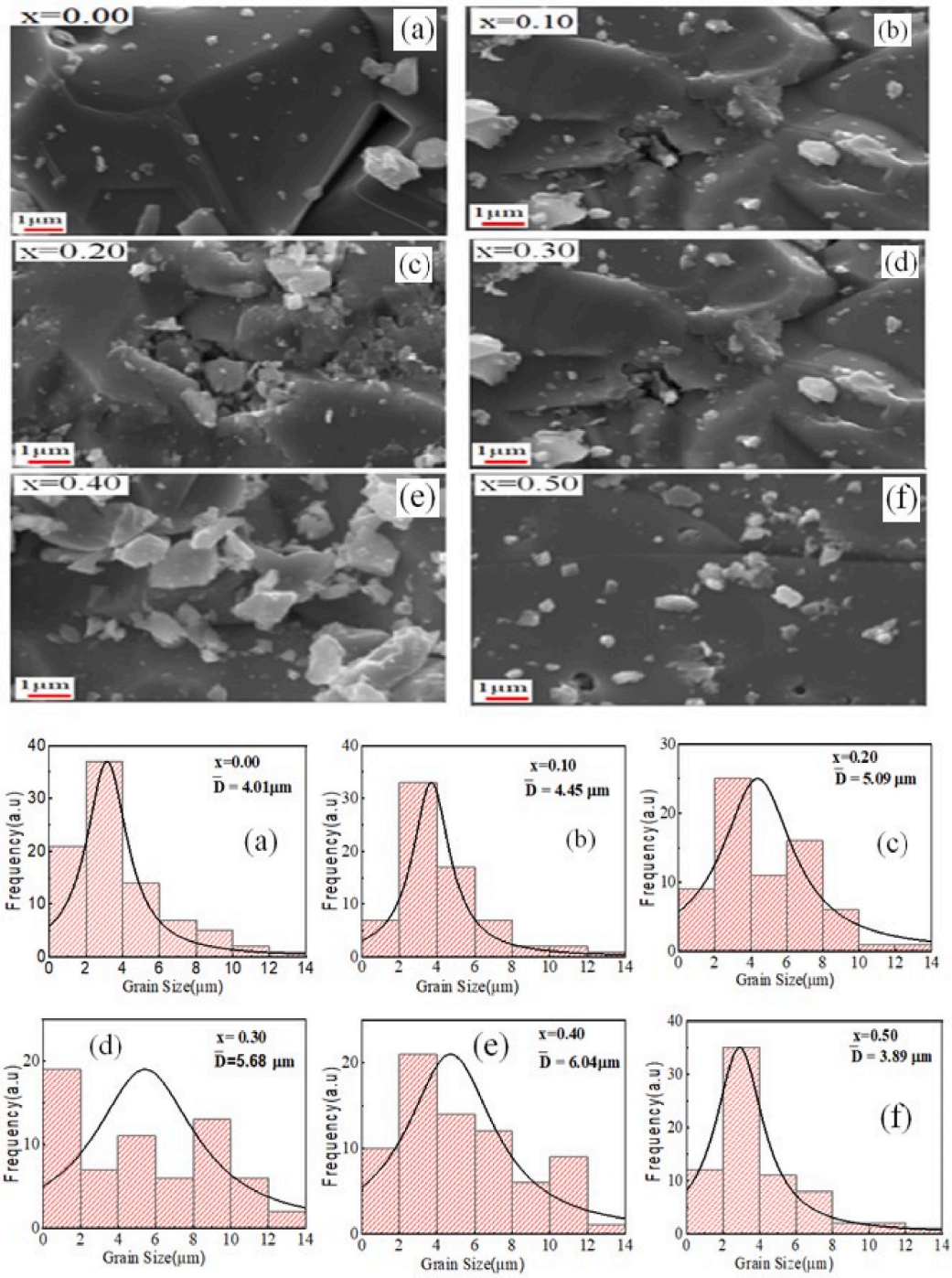

Fig. 3. (a–f) FESEM images along with grain distribution histograms for different Zn contents in $Li_{0.15}Ni_{0.6-x}Zn_xCu_{0.1}Fe_{2.15}O_4$ ferrites.

sharper peak, and of all the compositions being studied, the $x = 0.40$ composition shows the highest RQF value, about 3000. The investigated samples exhibit a broad frequency band that is important for practical applications.

Fig. 9 shows how the magnetic loss factor ($\tan\delta_M$) varies with frequency. The amount of energy loss in the system is represented by the $\tan\delta_M$. As the frequency increases, there is a notable drop in the values of $\tan\delta_M$, resulting in a higher frequency corresponding to lower $\tan\delta_M$ values. This is possibly due to the development of fewer imperfections and defects at a higher frequency. The motion of the domain wall is influenced by changes in the external magnetic field at low frequencies. Nevertheless, as the frequency is increased, the domain wall loses its ability to follow variations in the external magnetic field and may be approximated as having a constant $\tan\delta_M$

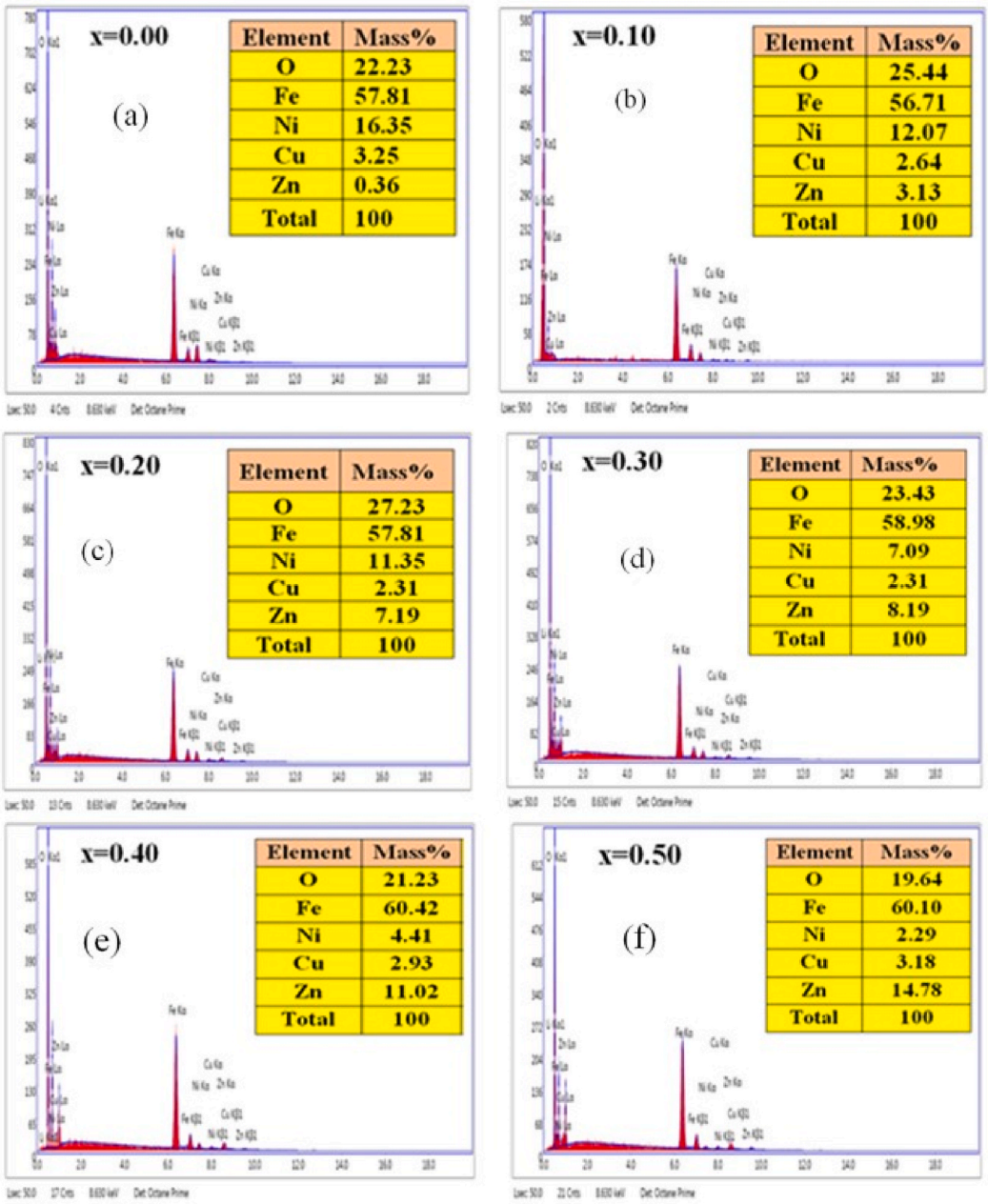

Fig. 4. (a–f) EDS spectrum for different Zn contents in $Li_{0.15}Ni_{0.6-x}Zn_xCu_{0.1}Fe_{2.15}O_4$ ferrites.

value. However, defects such as domain wall bending, non-uniform motion, fluctuations in localized flux density, annihilation, and nucleation contribute to the $\tan\delta_M$, which results from a lack of domain wall motion with an applied alternating current field [46].

3.6. $M - H$ hysteresis loops

Fig. 10 illustrates the variation in magnetization (M) with the applied magnetic field (H) for different ferrites. When the applied magnetic field (H) is introduced, the magnetization (M) of all compositions exhibits a linear rise until it reaches 0.142T, after which it approaches the saturation magnetization (M_s). The study reveals that the values of μ_i' and M_s exhibit a rising trend as the Zn doping level rises until reaching $x = 0.40$, after which they experience a subsequent decline. The variation of M_s with doping concentration can be explained by considering the cation distribution and the super-exchange interaction between tetrahedral (A) sites and octahedral (B) sites. It is known that Zn^{2+} (non-magnetic) occupies the A-sites and Li^{1+} (non-magnetic), Cu^{2+} (magnetic moment, $M_B = 1\mu_B$), and Ni^{2+} ($M_B = 2\mu_B$) occupy the B-sites. Conversely, Fe^{3+} (with a magnetic moment of 5 μB) can be occupied at both the A- and B-sites

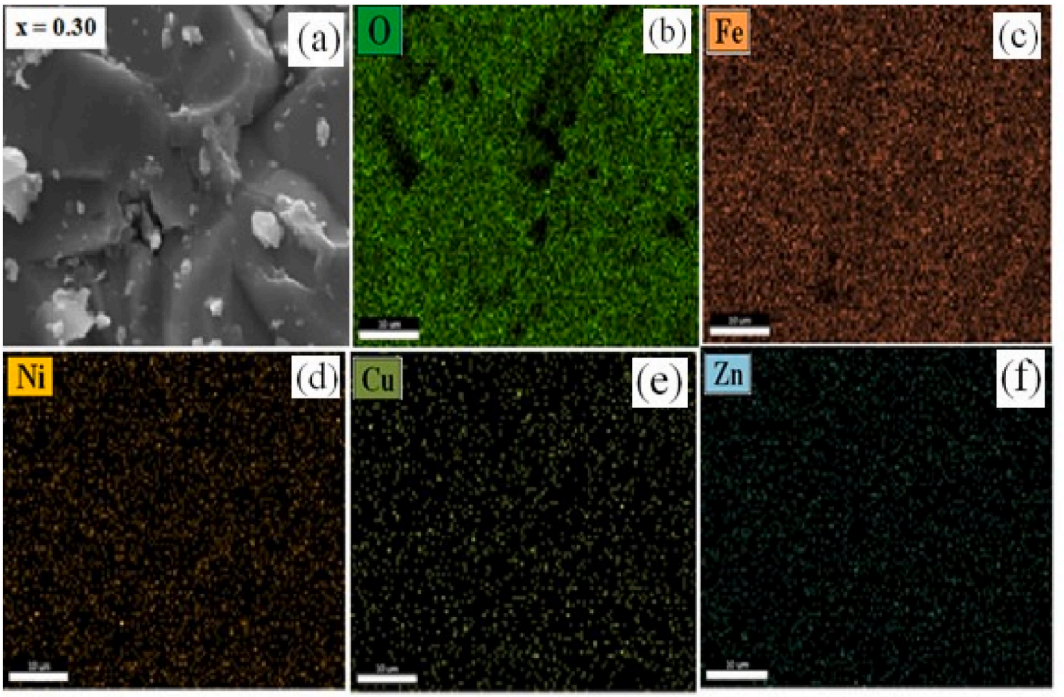

Fig. 5. (a) FESEM image for $x = 0.30$ sample, and (b–f) Element mapping for $x = 0.30$ sample.

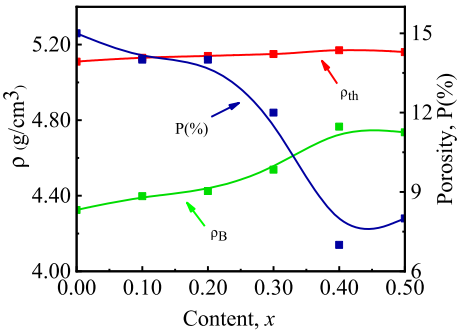

Fig. 6. The variation of ρ_{th}, ρ_B, and P with Zn content for $Li_{0.15}Ni_{0.6-x}Zn_xCu_{0.1}Fe_{2.15}O_4$ ferrites.

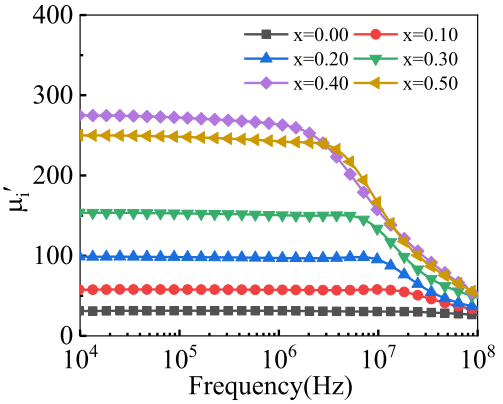

Fig. 7. Variation of μ_i' with frequency for different $Li_{0.15}Ni_{0.6-x}Zn_xCu_{0.1}Fe_{2.15}O_4$ ferrites.

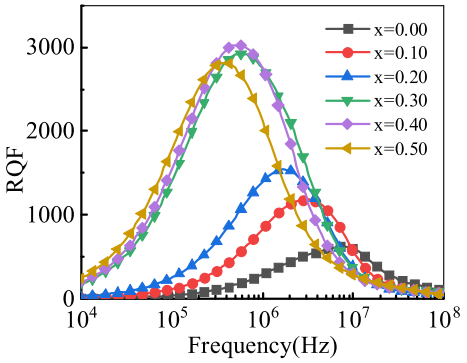

Fig. 8. Variation of RQF with frequency for various $Li_{0.15}Ni_{0.6-x}Zn_xCu_{0.1}Fe_{2.15}O_4$ ferrites.

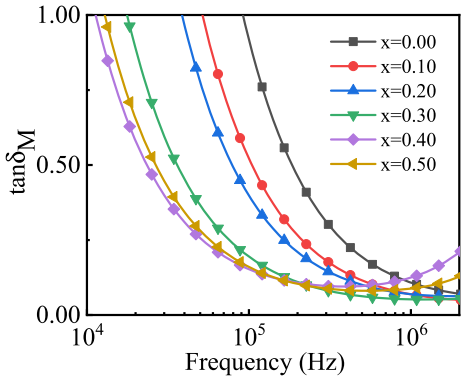

Fig. 9. Variation of $\tan\delta_M$ with frequency for different $Li_{0.15}Ni_{0.6-x}Zn_xCu_{0.1}Fe_{2.15}O_4$ ferrites.

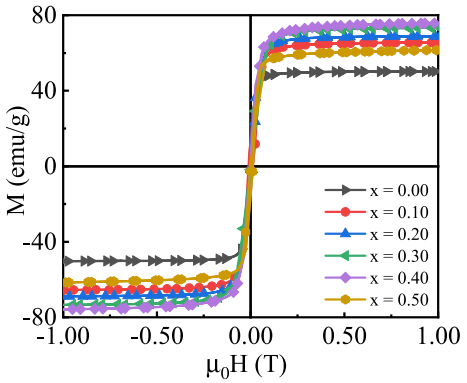

Fig. 10. M − H loop for various $Li_{0.15}Ni_{0.6-x}Zn_xCu_{0.1}Fe_{2.15}O_4$ ferrites.

[47–49]. In the current investigation, the probable arrangement of cations may be expressed as:

$$(Zn_x^{2+}Fe_{1-x}^{3+})_A\ [Li_{0.15}^{1+}Cu_{0.10}^{2+}Ni_{0.60-x}^{2+}Fe_{1.15+x}^{3+}]_BO_4 \quad (1)$$

where in equation (1), parenthesis () denotes tetrahedral A-sites and square brackets [ ] octahedral B-sites. Néel's two-sub-lattice model shows that A-B super-exchange interaction dominates intra-sub-lattice A-A and B–B interaction and that M_s corresponds to the vector sum of the magnetic moment of the individual's A- and B-sub lattices.

$$M_s = M_B\text{-}M_A = (6.78 + 3x\text{-}5 + 5x)\mu_B = (1.78 + 8x)\mu_B \quad (2)$$

where

$$M_B = [(0.1 \times 1) + (0.6\text{-}x)2 + 5(1.15 + x)]\mu_B = (6.78 + 3x)\mu_B \quad (3)$$

and

$$M_A = 5(1 - x)\mu_B = (5 - 5x)\mu_B \quad (4)$$

Thus, from equation (2), (3), and (4), it is evident that M_s should rise along with Zn concentration. The maximum value of M_s ($\sim$ 77.49 emu/g) is found for the $x = 0.40$ sample. A similar outcome has been previously reported [50]. However, beyond $x = 0.40$, Zn^{2+} may partly occupy the B-site, raising Fe^{3+} in the A-site and resulting in a drop in M_s [51,52]. Moreover, according to the Globus model, M_s is directly proportional to μ_i' [53,54]. As a result, M_s changes in the same way as μ_i' does. In addition, following the three sub-lattice models proposed by Yafet and Kittel, the observed drop in the saturation magnetization (M_s) beyond the composition $x = 0.40$ might potentially be attributed to the presence of non-collinear spin configurations [55].

3.7. Dielectric properties

The ε' vs. frequency graph is shown in Fig. 11. The high value of ε' is present at lower frequencies. As frequency increases, ε' rapidly decreases and becomes nearly insensitive to frequency in the high-frequency range. The Maxwell-Wagner and Koops phenomenological theories have been used to describe this type of dielectric behavior in ferrites [56–58]. Following the Maxwell-Wagner double-layer model the inhomogeneous dielectric structure of the substance causes space charge polarization [46,56]. In this concept, it is hypothesized that thin, poorly conducting grain boundaries separate highly conducting grains to generate a dielectric medium. Grains have enhanced efficacy at higher frequencies, whereas grain boundaries exhibit greater efficacy at lower frequencies. Similar findings are reported earlier [59–66].

As frequency rises, polarization falls until it reaches a definite value. The drop in ε' with frequency is due to the electronic interaction between Fe^{2+} and Fe^{3+} ions not following the AC field frequency above a certain frequency. Since the grain boundaries have very high resistance, electrons traveling along them create a significant space charge polarization. Consequently, the value of ε' has a large magnitude in the low-frequency range. As the frequency increases, the electrons undergo rapid changes in direction, resulting in a decrease in their velocity inside the dielectric material. Consequently, this phenomenon leads to a reduction in the accumulation of charge at the interfaces between the grains. The decline in space charge polarization leads to a decrease in the values of ε' [67]. The maximum ε' ($\sim 2.85 \times 10^3$) is observed for the $x = 0.10$ sample.

It is thought that two mechanisms (electron hopping and charged defect dipoles) are the basis of the $\tan\delta_E$ in ferrites. The fundamental cause of $\tan\delta_E$ is the rotational motion of electrons. The presence of impurities and defects inside the crystal lattice may result in a lag between the polarization and the applied alternating current (AC) field, leading to the occurrence of $\tan\delta_E$. The variation of the $\tan\delta_E$ is greatly influenced by the density of the material. Fig. 12 shows the anomalous behavior in the frequency response of $\tan\delta_E$, which may be due to the resonance effect. The presence of both negative and positive charge carriers may be responsible for this anomalous behavior [68]. There are noticeable relaxation peaks due to the different concentrations of Fe^{2+} ions that were produced throughout the sintering procedure. Additionally, when the externally applied AC field is about equivalent to the localized electrons' jumping frequency these peaks appear. These resonant $\tan\delta_E$ peaks are observed in the spinel ferrites when the relation $\omega\tau = 1$, is satisfied, where $\omega = 2\pi f$ [69].

3.8. Impedance studies

Impedance spectroscopy is useful for investigating the effect of different constituents on polycrystalline materials, especially at interfaces, grains, and grain boundaries. Information about resistive and reactive components is statistically provided by the impedance measurements. Fig. 13 illustrates two components of impedance, namely the real portion (Z′) and the imaginary part (Z″), as a function of frequency for all the samples. Both Z' and Z'' decrease with increasing frequency demonstrating that the applied AC field promotes conduction. Fig. 13(a) shows that the Z' exhibits a high dispersion in the low-frequency range, followed by a plateau. The

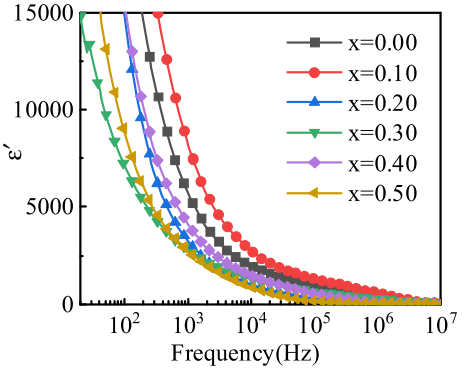

Fig. 11. Variation of ε' with frequency for $Li_{0.15}Ni_{0.6\text{-}x}Zn_xCu_{0.1}Fe_{2.15}O_4$ ferrites.

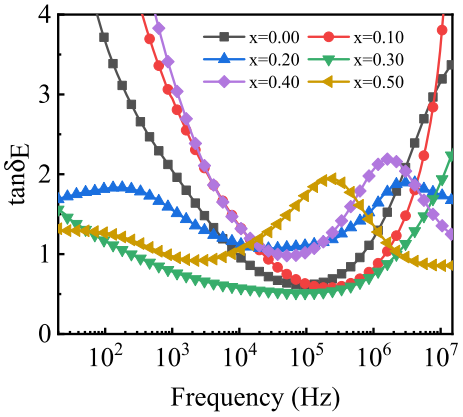

Fig. 12. Variation of $\tan\delta_E$ as a function of frequency for various LNZCFO ferrites.

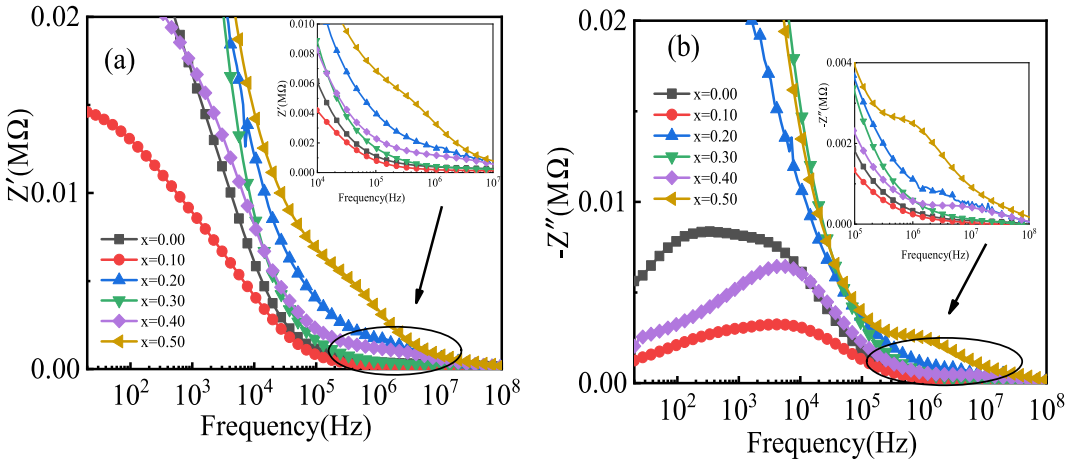

Fig. 13. Variation of (a) Z', and (b) Z'' with frequency for various $Li_{0.15}Ni_{0.6-x}Zn_xCu_{0.1}Fe_{2.15}O_4$ ferrites.

behavior of each curve eventually approaches zero as the frequency increases, suggesting that Z' exhibits frequency frequency-independent nature. At higher frequencies, the rate of recombination increases while the relaxation of the space charge slows down. Consequently, the polarization of the space charge declines, leading to the merging of the curves seen in all the samples. The patterns of Z'' curves show similar behavior as Z' (shown in Fig. 13(b)). The peaks in the Z'' curve are observed at lower frequencies for some samples and may be attributable to oxygen vacancies or space charge relaxation of immobile charges [70–72].

Impedance spectroscopy is a well-recognized technique used for the assessment of the impact of grain and grain boundary effects on polycrystalline materials. The Nyquist plots are well-suited for materials that exhibit one or more distinct relaxation processes of comparable amplitude and follow the Cole-Cole functional approaches. The plot may have two semi-circles depending on the electrical characteristics of the material. The semicircular arc seen in the lower frequency range corresponds to the resistance associated with the grain boundary. Conversely, the subsequent semicircular arc observed in the higher frequency area indicates the resistance associated with the grain itself [73]. The prominent grain boundary effect arises from the parallel alignment of the resistance and capacitance of the grains in the material. Instead, grain impact is caused by parallel grain resistance and capacitance within the sample [74]. Fig. 14 shows the Nyquist plots of the studied samples fitted by using ZSimpWin software. The plotted complex impedance is related to the following relation,

$$Z^* = Z^{'} + iZ^{''} \tag{5}$$

in equation (5), Z^* is the complex impedance of the samples. From Fig. 14(c) it is evident that the $x = 0.20$ and $x = 0.40$ samples exhibit two partly semi-circles, indicating the significant effect of both grain and grain boundary on the conduction process of these samples. Less than two orders of magnitude separate the relaxation periods of the relaxation processes associated with the conduction of grains and grain borders. For these samples the Nyquist plots are well matched with the suitable equivalent circuit configuration ($R_g//C_g + R_{gb}//C_{gb}$) showed in Fig. 14(a), where, R_g, C_g, R_{gb}, and C_{gb} are the grain resistance, grain capacitance, grain boundary resistance, and grain boundary capacitance respectively [75–78]. It is also observed that samples with $x = 0.00$, 0.10, 0.30, and 0.50 exhibit only a

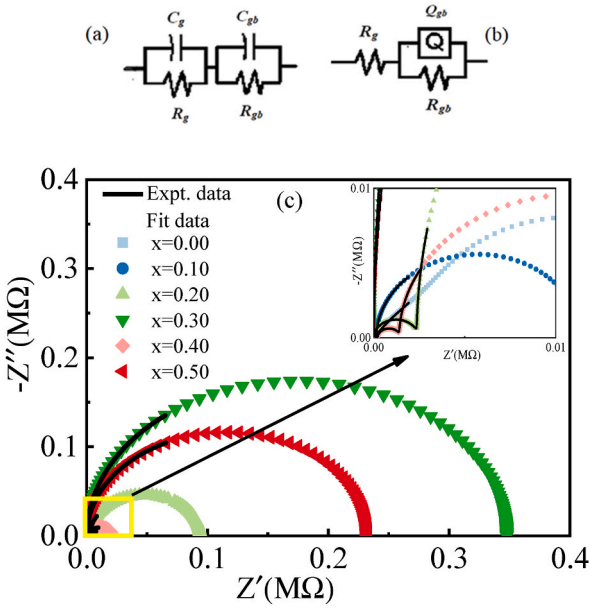

Fig. 14. (a&b) Circuit diagrams, and (c) Nyquist fitting plot for different $Li_{0.15}Ni_{0.6-x}Zn_xCu_{0.1}Fe_{2.15}O_4$ ferrites.

single semicircular arc in the low-frequency areas, indicating that only the grain boundary is prominent for the conduction mechanism [79]. The Randles circuit configuration for the above-mentioned ferrites is ($R_g + R_{gb}//Q_{gb}$) shown in Fig. 14(b), here the term Q_{gb} represents the phase element of the grain boundary. The values of R_{gb} are more influential than the R_g because the grain boundary contributes to the conduction mechanism at the lower frequency region. The constant phase element (Q_{gb}) can be given as, $ZQ_{gb} = 1/Q(j\omega)^{\alpha}$, where Q and α do not depend on frequency indicating the constant phase element parameter [80–82]. It also observed that the non-Debye relaxation mechanism of dielectric material is dominant for the samples since the center of the semicircle is located above or below the Z' axis [83–86].

3.9. Electric modulus

Electric modulus spectroscopy is used to characterize the electrical relaxation of spinel ferrite and determine the function of the grain and the grain boundaries in the conduction process [87]. Fig. 15 represents the frequency-dependent behavior of (a) the real part (M') and (b) the imaginary part (M'') of the electric modulus for the investigated samples. In Fig. 15(a), the magnitude of M' exhibits a sharp rise as frequency increases, while remaining relatively constant at lower frequencies with values approaching zero. This behavior

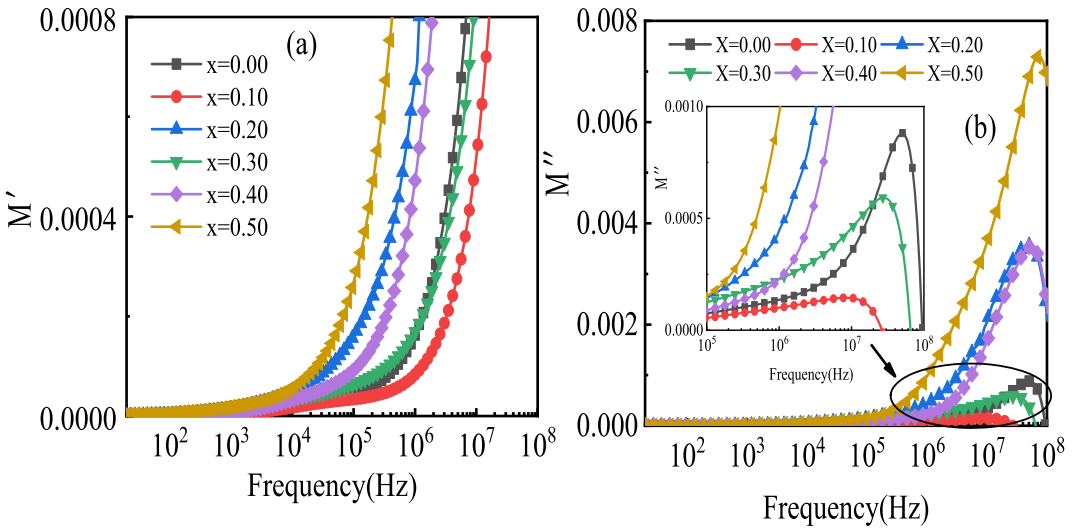

Fig. 15. Variation of (a) M', and (b) M'' with frequency for various $Li_{0.15}Ni_{0.6-x}Zn_xCu_{0.1}Fe_{2.15}O_4$ ferrites.

indicates the negligible contribution of electronic polarization at higher frequencies. When the frequency is increased to a high magnitude, the value of M' exhibits a rapid increase, suggesting that charge carriers are undergoing conduction across short distances [88,89]. The variation of M'' with frequency is shown in Fig. 15(b). At lower frequencies, the value of M'' is very low. However, when the frequency range of 10^6–10^7 Hz is reached, strong peaks are noticed. These peaks are associated with the relaxation process and may be credited to the contribution of grains. The contribution of these grains is connected to the relaxation peak located at the high-frequency region [71,72]. The relaxation frequency is denoted by the frequency at which the value of M'' is maximal (at peak point). Charge carriers in the high-frequency zone do not follow AC fields because they are restricted within potential wells, travel small distances, and decline to lower values of M'' as frequency increases [90]. The peak specifies a shift from long-distance to short-distance mobility of charge charier. Asymmetrical peak broadening at both maxima supports the concept that relaxation times are diverse time constants [91].

3.10. The ac conductivity

Fig. 16(a) displays the frequency-dependent variations of σ_{ac}. Each composition demonstrates a frequency-independent characteristic until it reaches a frequency of 10^4 Hz, where it behaves similarly to a direct current (DC) conductive material. However, the σ_{ac} increases sharply as the frequency rises. According to Austin and Mott's polaron hopping methods, a rising trend of ac indicates small polaron hopping, whereas a decreasing trend indicates large polaron hopping [92]. Thereby, small polaron hopping is observed in the present study. The increase in σ_{ac} is caused by electron exchange between ions of the same element with different valence states. The Maxwell-Wagner double-layer model may also be used to describe this phenomenon [93,94]. According to this model, when frequency increases, grain activity increases, promoting electron hopping between two adjacent octahedral sites, facilitating the Fe^{3+} to Fe^{2+} ion transition, and eventually contributing to the σ_{ac} mechanism.

Fig. 16(b) shows the variation of $\log\sigma_{ac}$ vs. $\log\omega$. The $\log\sigma_{ac}$ grows literally linearly with frequency, indicating that the conduction process is caused by the small polaron hopping mechanism in all samples. According to Jonscher's power law, the relationship between $\log\sigma_{ac}$ vs. $\log\omega$ should be linear. However, a little deviation is found due to the existence of mixed (small/large) polarons [86,95,96].

4. Conclusions

The solid-state reaction method is used for the synthesis of various $Li_{0.15}Ni_{0.6-x}Zn_xCu_{0.1}Fe_{2.15}O_4$ ferrites. The XRD patterns confirm the existence of a singular-phase cubic spinel structure of the studied samples. The densities and $\overline{D}$ values of the ferrites show a significant increase as the Zn concentration rises, whereas the porosity exhibits a contrary behavior. The substitution of Zn content results in the formation of a high magnetic phase, hence improving the homogeneity and interaction between magnetic grains. This enhancement leads to an increase in μ_i' and a decrease in magnetic loss. The highest values of μ_i' and RQF ($\mu_i' = 276$ and RQF=3000) are found for the $x = 0.4$ sample. The magnetization also increases with Zn concentration and the highest value of M_s (~ 77.49 emu/g) is found for $x = 0.40$ composition. The optimum ε' ($\sim 2.85 \times 10^3$) is found for the $x = 0.10$ sample. The inconsistent behavior of $\tan\delta_E$ with relaxation peaks in the compositions may be attributed to the resonance effect and varying mobility of the charge carriers. The values of Z' and Z'' exhibit a decreasing trend as the frequency increases, indicating that the applied AC field facilitates the conduction of the material. The semi-circles in the Nyquist plot prove the existence of non-Debye-type dielectric relaxation. The modulus and σ_{ac}

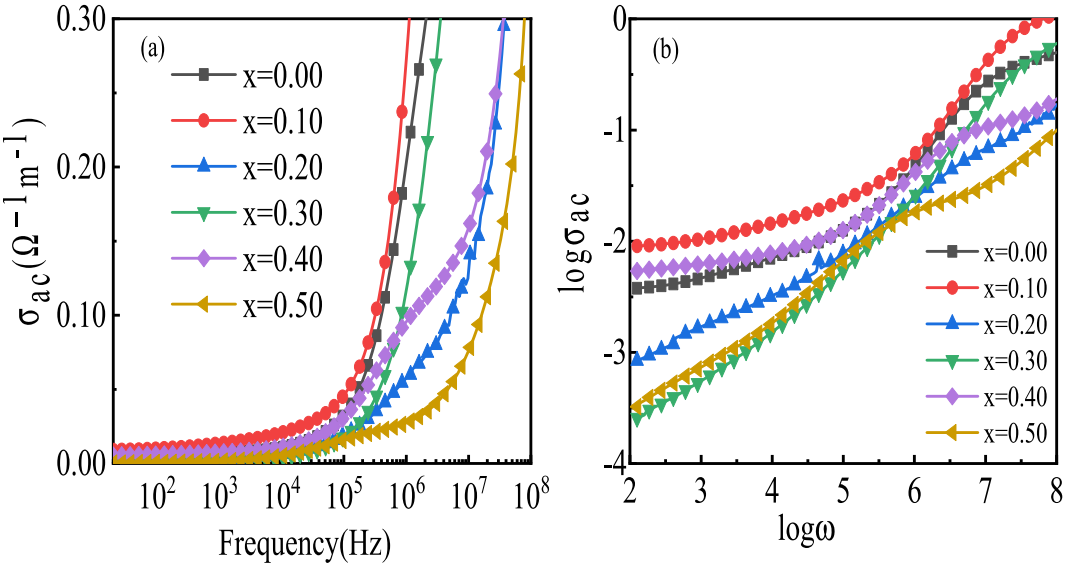

Fig. 16. (a) Frequency dependence σ_{ac}, and (b) $\log\sigma_{ac}$ vs. $\log\omega$ for different for $Li_{0.15}Ni_{0.6-x}Zn_xCu_{0.1}Fe_{2.15}O_4$ ferrites.

for the investigated compositions result from the polaron hopping process. Small polaron hopping and lattice strain caused by free charges both contribute to the linear increase in $\log\sigma_{ac}$ with $\log\omega$. The novelty of the present study is that composition $Li_{0.15}Ni_{0.2}Zn_{0.4}Cu_{0.1}Fe_{2.15}O_4$ has a high M_s ($\sim$ 77.49 emu/g), making them a viable alternative to Pb-based materials for the application of modern multifunctional devices.

Data availability statement

No. The data that has been used is confidential.

Ethics declarations

Review and/or approval by an ethics committee was not needed for this study because it is an experimental work in the field of material science.

CRediT authorship contribution statement

Jannatul Ferdaus: Data curation, Formal analysis, Investigation, Methodology, Writing – original draft, Writing – review & editing. **Mithun Kumar Das:** Conceptualization, Data curation, Formal analysis, Funding acquisition, Investigation, Methodology, Project administration, Resources, Software, Supervision, Validation, Visualization, Writing – original draft, Writing – review & editing. **Anamika Dey:** Data curation, Formal analysis, Investigation. **Bablu Chandra Das:** Formal analysis, Writing – review & editing. **F. Alam:** Formal analysis, Investigation. **Mashudur Rahaman:** Data curation, Resources. **Md Azizul Hoque:** Investigation, Resources. **Muhammad Shahriar Bashar:** Investigation, Resources.

Declaration of competing interest

The authors declare that they have no known competing financial interests or personal relationships that could have appeared to influence the work reported in this paper.

Acknowledegments

The authors are grateful to Comilla University, Cumilla-3506, Bangladesh, and Bangladesh Council of Scientific and Industrial Research (BCSIR), Dhaka.

References

[1] Alex Goldman, Modern Ferrite Technology, second ed., Springer Science+Business Media, Inc., Van Nostrand Reinhold, New York, 1990 https://doi.org/10.1007/978-0-387-29413-1.
[2] L.G. Vanuitert, High resistivity nickel ferrites-the effect of minor additions of manganese or cobalt high-resistivity nickel ferrites-the effect of minor additions of manganese or cobalt, J.Chem.Phy. 306 (1956) 8–13, https://doi.org/10.1063/1.1742468.
[3] E.J.W. Verwey, J.H. De Boer, Cation arrangement in a few oxides with crystal structure, Rec.Trav. Chim 55 (1936) 531–540, https://doi.org/10.1002/recl.19360550608.
[4] M. Srikanth, P. Easwaraji, A study of electrical and magnetic properties of Cu substituted Ni-Zn Ferrites, IOSR J. Appl. Phys. 8 (2016) 34–39, https://doi.org/10.1142/S0217984914502443.
[5] Guang-sheng Luo, Yu-hao Hong, Wei-ping Zhou, et al., Effect of chromium substitution on structural, electrical and magnetic properties of Ni-Zn ferrites, Trans. Nonferrous Metals Soc. China 30 (2020) 1895–1903, https://doi.org/10.1016/S1003-6326(20)65348-1.
[6] G.S. Luo, W.P. Zhou, J.D. Li, The influence of Nd^{3+}ions doping on structural,dielectric and magnetic properties of Ni-Zn ferrites, J. Mater. Sci. Mater. Electron. 28 (2017) 7259–7263, 10.1007/s10854-017-6408-6.
[7] S.E. Jacobo, P.G. Bercoff, Structural andelectromagnetic properties of yttrium-substituted Ni−Zn ferrites, Ceram. Int. 42 (2016) 7664–7668, https://doi.org/10.1016/j.ceramint.2016.01.180.
[8] Guang-sheng Luo, Wei-ping Zhou, Jian-de Li, Gui-wen Jiang, Effect of Cu ion substitution on structural and dielectric properties of Ni-Zn ferrites, Trans. Nonferrous Metals Soc. China 25 (2015) 3678–3684, https://doi.org/10.1016/S1006-6326(15)64077-8.
[9] Sea-Fue Wang, Yung-Fu Hsu, Kai-Mou Chou, Jeng-Ting Tsai, Effects of co-dopants on the magnetic properties of Ni-Zn ferrites, J. Magn. Magn Mater. 374 (2015) 402–410, https://doi.org/10.1016/j.jmmm.2014.08.075.
[10] S. Ikram, J. Jacob, M.I. Arshad, K. Mahmood, A. Ali, Tailoring the structural, magnetic and dielectric properties of Ni-Zn-$CdFe_2O_4$ spinel ferrites by the substitution of lanthanum ions, Ceram. Int. 45 (2019) 3563–3569, https://doi.org/10.1016/j.ceramint.2018.11.015.
[11] M. Junaid, M.A. Khan, M.N. Akhtar, Impact of Indium substitution on dielectric and magnetic properties of $Cu_{0.5}Ni_{0.5}Fe_{2-x}O_4$ ferrite materials, Ceram. Int. 45 (2019) 13431–13437, https://doi.org/10.1016/j.ceramint.2019.04.042.
[12] J.J. Shrotri, Effect of Cu substitution on the magnetic and electrical properties of Ni-Zn ferrite synthesized by soft chemical method, Mater. Chem. Phys. 59 (1999) 1–5, https://doi.org/10.1016/S0254-0584(99)00019-X.
[13] H. Su, H.W. Zhang, X.L. Tang, L.J. Jia, Q.Y. Wen, Sintering characteristics and magnetic properties of NiCuZn ferrites for MLCI applications, Mater. Sci. Eng. B 129 (2006) 172–175, https://doi.org/10.1016/j.mseb.2006.01.008.
[14] C.L. Miao, J. Zhou, X.M. Cui, X.H. Wang, Z.X. Yue, L.T. Li, Cofiring behavior and interfacial structure of NiCuZn ferrite/PMN ferroelectrics composites for multilayer LC filters, Mater. Sci. Eng. B 127 (2006) 1–5, https://doi.org/10.1016/j.mseb.2005.04.024.
[15] C. Miclea, C. Tanasoiu, C.F. Miclea, A. Gheorghiu, V. Tanasiou, Soft ferrite materials for magnetic temperature transducers and applications, J. Magn. Magn Mater. 290 (2005) 1506–1509, https://doi.org/10.1016/j.jmmm.2004.11.561.
[16] N. Rezlescu, C. Doroftei, P.D. Popa, Structure and humidity sensitive electrical properties of the Sn^{4+} and/or Mo^{6+} substituted Mg ferrite, Sens. Actuators B Chem. 115 (2006) 589–595, https://doi.org/10.1016/j.snb.2005.10.028.
[17] D. Stoppels, Developments in soft magnetic power ferrites, J. Magn. Magn Mater. 160 (1996) 323–328, https://doi.org/10.1016/0304-8853(96)00216-8.

[18] H.M. Sung, C.J. Chen, L.J. Wang, W.S. Ko, The characteristics of low temperature co-fired multilayer chip LC filters, IEEE Trans. Magn. 34 (1998) 1363–1365, https://doi.org/10.1109/20.706549.

[19] S.M. Hoque, M.A. Choudhury, M.F. Islam, Characterization of Ni-Cu mixed spinel ferrite, J. Magn. Magn Mater. 251 (2002) 292–303, https://doi.org/10.1016/S0304-8853(02)00700-X.

[20] S. Akhter, M.A. Hakim, Magnetic properties of cadmium substituted lithium ferrites, Mater. Chem. Phys. 120 (2010) 399–403, https://doi.org/10.1016/j.matchemphys.2009.11.023.

[21] S. Verma, P.A. Joy, Magnetic properties of superparamagnetic lithium ferrite nanoparticles, J. Appl. Phys. 98 (2005), 124312, https://doi.org/10.1063/1.2149493.

[22] R. Parvin, A.A. Momin, A.K.M. Akther Hossain, Improvement of microstructure, initial permeability, magnetization and dielectric properties of nanocrystalline $Li_xCu_{0.1}Co_{0.1}Zn_{0.8-2x}Fe_{2+x}O_4$, J. Magn. Magn Mater. 401 (2016) 760–769, https://doi.org/10.1016/j.jmmm.2015.10.130.

[23] Kin O. Low, Frank R. Sale, The development and analysis of property-composition diagrams on gel-derived stoichiometric NiCuZn ferrite, J. Magn. Magn Mater. 256 (2003) 221–226, https://doi.org/10.1016/S0304-8853(02)00482-1.

[24] G. Goev, V. Masheva, L. Ilkov, D. Nihtianova, M. Mikhov, Proceedings of the fifth General Conference of the Balkan Physical Union BPU-5 687 (2003).

[25] M. Ajmal, A. Maqsood, Structural, electrical and magnetic properties of $Cu_{1-x}Zn_xFe_2O_4$ ferrites ($0 \leq x \leq 1$), J. Alloys Compd. 460 (2008) 54–59, https://doi.org/10.1016/j.jallcom.2007.06.019.

[26] S.A. Jadhav, Structural and magnetic properties of Zn substituted Li-Cu ferrites, Mater. Chem. Phys. 65 (2000) 120–123, https://doi.org/10.1016/S0254-0584(00)00221-2.

[27] M.A. Islam, M.M. Hasan, A.K.M. Akther Hossain, Enhancement of initial permeability and reduction of loss factor in Zn substituted nanocrystalline $Li_{0.35-0.5x}Ni_{0.}Zn_xFe_{2.35-0.5x}O_4$, J. Magn. Magn Mater. 424 (2017) 108–114, https://doi.org/10.1016/j.jmmm.2016.10.030.

[28] R.G. Gupta, R.G. Mendiratha, Mössbauer studies in $Zn_xMn_{1-x}Fe_2O_4$ systems" J Appl Phys. 48 (1977) 845–848, https://doi.org/10.1063/1.323642.

[29] A. Goldman, Handbook of modern ferromagnetic materials, Kluwer Academic Publishers, Boston, U.S.A, 1999.

[30] B.D. Cullity, C.D. Graham, Introduction to magnetic materials, second ed., Wiley-IEEE Press, Hoboken, New Jersey, USA, 2008.

[31] A.J. Moulson, J.M. Herbert, Electroceramics: Materials, Properties, and Application", Chapman & Hall, UK, 1990.

[32] R. Grossinger, G.V. Duong, R. Sato-Turtelli, The physics of magnetoelectric composites, J. Magn. Magn Mater. 320 (2008) 1972–1977, https://doi.org/10.1016/j.jmmm.2008.02.031.

[33] A. Patterson, The scherrer formula for X-ray particle size determination, Phys. Rev. 56 (1939) 978–982, https://doi.org/10.1103/PhysRev.56.978.

[34] L. Vegard, Magnetic properties of Ni-Zn ferrites by citrate gel method, Z. Phys. 5 (1921) 17.

[35] R.D. Shannon, C.T. Prewitt, Revised values of effective ionic radii, ActaCrystallogr 26 (1970) 1046–1048, https://doi.org/10.1107/S0567740870003576.

[36] Sadaf Bashir Khan, Syed Irfan, Shern Long Lee, Influence of Zn^{+2} doping on Ni-based nanoferrites; ($Ni_{1-x}Zn_xFe_2O_4$), Nanomaterials 9 (2019) 1024, https://doi.org/10.3390/nano9071024.

[37] Vinay DeshrajMeena, Kumar Verma, ShilpaRana DivyaPrerna, Investigation the effect of Zn doping on structural and optical properties of SnO_2, Mater. Today Proc. 51 (2022) 554–560, https://doi.org/10.1016/j.matpr.2021.05.676.

[38] M. Derakhshani, E. Taheri-Nassaj, M. Jazirehpour, Structural, magnetic, and gigahertz-range electromagnetic wave absorption properties of bulk Ni-Zn ferrite, Sci. Rep. 11 (2021) 9468, https://doi.org/10.1038/s41598-021-88930-0.

[39] D.V. Kurmude, A.B. Shinde, A.A. Pandit, C.M. Kale, D. R Shengule, K.M. Jadhav, X-ray and infrared studies on superparamagnetic Ni-Zn ferrite nanocrystals, J. Supercond. Nov. Magnetism 28 (2015) 1759–1766, https://doi.org/10.1007/s10948-014-2943-z.

[40] G. Nabiyouni, M. J AfariFesharaki, M. Mozafari, J. Amighian, Characterization and magnetic properties of nickel ferrite nanoparticles prepared by ball milling technique, Chin. Phys. Lett. 2 (2010), 126401, https://doi.org/10.1088/0256-307X/27/12/126401.

[41] A.A. Sattar, H.M. El-Sayed, K.M. El-Shokrofy, M.M. El-Tabey, Improvement of the magnetic properties of Mn-Ni-Zn ferrite by the non-magnetic Al^{3+}Ion substitution, J. Appl. Sci. 5 (2005) 162–169, https://doi.org/10.3923/jas.2005.162.168.

[42] A. Globus, P. Duplex, M. Guyot, Determination of initial magnetization curve from crystallites size and effective anisotropy field, IEEE Trans. Magn. 7 (1971) 617–622, https://doi.org/10.1109/TMAG.1971.1067200.

[43] J.L. Snoek, Dispersion and absorption in magnetic ferrites at frequencies above one Mc/s, Physica 14 (1948) 207–217, https://doi.org/10.1016/0031-8914(48)90038-X.

[44] T. Nakamura, Snoek's limit in high-frequency permeability of polycrystalline Ni-Zn, Mg-Zn, and Ni-Zn-Cu spinel ferrites, J. Appl. Phys. 88 (2000) 348–353, https://doi.org/10.1063/1.373666.

[45] T. Tsutaoka, M. Ueshima, T. Tokunaga, T. Nakamura, K. Hatakeyama, Frequency dispersion and temperature variation of complex permeability of Ni-Zn ferrite composite materials, J. Appl. Phys. 78 (1995) 3983–3991, https://doi.org/10.1063/1.359919.

[46] M. Manjurul Haque, M.A. Hakim, Influence of CuO and sintering temperature on the microstructure and magnetic properties of Mg-Cu-Zn ferrites, J. Magn. Magn Mater. 320 (2008) 2792–2799, https://doi.org/10.1016/j.jmmm.2008.06.017.

[47] J. Smith, Magnetic Properties of Materials, Mc-Graw Hill, New York, 1971.

[48] S.A. Jadhav, Magnetic properties of Zn-substituted Li-Cu ferrites, J. Magn. Magn Mater. 224 (2001) 167–172, https://doi.org/10.1016/S0304-8853(00)00580-1.

[49] A.M. Sheikh, S.C. Watae, S.A. Jadhav, B.K. Chougule, Preparation and characterization of Zn substituted Li-Mg ferrites, Mater. Res. Bull. 37 (2002) 2547–2555, https://doi.org/10.1016/S0025-5408(02)00744-4.

[50] Mithun Kumar Das, Bablu Chandra Das, S.C. Mazumdar, M.N.I. Khan, Hidekazu Tanaka, A.K.M. Akther Hossain, Rietveld refined crystal structure, magnetic, dielectric, and electric properties of Li- substituted Ni-Cu-Zn ferrite and Sm, Dy co-doped $BaTiO_3$ multiferroic composites, Ceram. Int. 49 (2023) 6045–6054, https://doi.org/10.1016/j.ceramint.2022.11.142.

[51] M.M. Ismail, N.A. Jaber, Dielectric properties of Li doped Ni-Zn ferrite, Iraq. J.Phys. 16 (2018) 140–152, https://doi.org/10.30723/ijp.v16i36.39.

[52] X. Wu, W. Chen, W. Wu, H. Li, C. Lin, Structural and magnetic properties evolution of Li-substituted $Co_{0.5}Ni_{0.5}Fe_2O_4$ ferrite, J. Electron. Mater. 46 (2017) 199–207, https://doi.org/10.1007/s11664-016-4877-7.

[53] A. Globus, P. Duplex, M. Guyot, Determination of initial magnetization curve from crystallites size and effective anisotropy field, IEEE Trans. Magn. 7 (1971) 617–622, https://doi.org/10.1109/TMAG.1971.1067200.

[54] A. Globus, P. Duplex, Separation of susceptibility mechanisms for ferrites of low anisotropy, IEEE Trans. Magn. 2 (1966) 441–445, https://doi.org/10.1109/TMAG.1966.1065867.

[55] Y. Yafet, C. Kittel, Antiferromagnetic arrangements in ferrites, Phys. Rev. 87 (1952) 290, https://doi.org/10.1103/PhysRev.87.290.

[56] J. Maxwell, A Treatise on Electricity and Magnetism, Clarendon Press, Oxford, London, 1982.

[57] K. Wangner, Annalende Physik, Leipzig, vol. 40, 1913, p. 817, https://doi.org/10.1002/andp.19133450502.

[58] C.G. Koops, On the dispersion of resistivity and dielectric constant of some semiconductors at audio frequencies, Phys. Rev. E 83 (1951) 121–124, https://doi.org/10.1103/PhysRev.83.121.

[59] M.M. Haque, M. Huq, M.A. Hakim, Densification, magnetic and dielectric behaviour of Cu-substituted Mg-Zn ferrites, Mater. Chem. Phys. 112 (2008) 580–586, https://doi.org/10.1016/j.matchemphys.2008.05.097.

[60] A. Ahad, M.A. Taher, Mithun Kumar Das, M.Z. Rahaman, M.N.I. Khan, Effect of Y substitution on magnetic and transport properties of $Ba_{0.95}La_{0.05}Ti_{1-x}Y_xO_3$ ceramics, Results Phys. 12 (2019) 1925–1932, https://doi.org/10.1016/j.rinp.2019.01.072.

[61] Z.X. Yue, Z. Ji, L.T. Li, X.L. Wang, Z.L. Gui, Effect of copper on the electromagnetic properties of Mg-Zn-Cu ferrites prepared by sol-gel auto-combustion method, Mater. Sci. Eng., B 86 (2001) 64–69, https://doi.org/10.1016/s0921-5107(01)00660-2.

[62] T. Ahamed, A. Ahad, Mithun Kumar Das, M.A. Taher, Mohammad J. Miah, M.N.I. Khan, Synthesis and characterization of dielectric, electric, and magnetic properties of vanadium doped-bismuth europium ferrites for multiferroic applications, Results Phys. 50 (2023), 106571, https://doi.org/10.1016/j.rinp.2023.106571.

[63] Z.X. Yue, Z. Ji, Z.L. Gui, L.T. Li, Magnetic and electrical properties of low-temperature sintered Mn-doped Ni-Cu-Zn ferrites, J. Magn. Magn Mater. 264 (2003) 258–263, https://doi.org/10.1016/s0304-8853(03)00214-2.

[64] S. Haque, S.C. Mazumdar, M.N.I. Knan, Mithun Kumar Das, Impact of Cr substitution on structural, magnetic, electric and impedance study of Mn-Ni-Zn ferrites, Mater. Sci. Appl. 12 (2021) 121–138, https://doi.org/10.4236/msa.2021.123008.

[65] Md Abu Mosa, M.K. Das, F. Alam, M.N.I. Khan, S.C. Mazumdar, Enhanced multiferroic properties in Ba and Sm codoped $BiFeO_3$ ceramics, J. Mater. Sci. Mater. Electron. 33 (2022) 25089–25102, https://doi.org/10.1007/s10854-022-09215-4.

[66] S. Akter, A. Ahad, Mithun Kumar Das, M.A. Taher, A. Barik, F. Alam, M.N.I. Khan, Study of structural, dielectric, and impedance properties of lead-free Zr and Y Co-doped $BaTiO_3$, Mater. Chem. Phys. 275 (2022), 125241, https://doi.org/10.1016/j.matchemphys.2021.125241.

[67] M. Aliuzzaman, M. Manjurul Haque, M. Jannatul Ferdous, S. Manjula Hoque, M.A. Hakim, Effect of sintering time on the structural, magnetic and electrical transport properties of $Mg_{0.35}Cu_{0.20}Zn_{0.45}Fe_{1.94}O_4$ ferrites, WJCMP 4 (2014) 13–23, https://doi.org/10.4236/wjcmp.2014.41003.

[68] D.K. Pradhan, R.N.P. Choudhary, C. Rinaldi, R.S. Katiyar, Effect of Mn substitution on electrical and magnetic properties of Bi0.9La0.1FeO3, J. Appl. Phys. 106 (2009), 024102, https://doi.org/10.1063/1.3158121.

[69] Y.D. Kolekar, L.J. Sanchez, C.V. Ramana, Dielectric relaxations and alternating current conductivity in manganese substituted cobalt ferrite, J. Appl. Phys. 115 (2014), 114106, https://doi.org/10.1063/1.4870232.

[70] B. Kaur, L. Singh, V. Annapu Reddy, D.Y. Jeong, N. Dabra, J.S. Hundal, AC impedance spectroscopy, conductivity and optical studies of Sr doped bismuth ferrite nano-composites, Int. J. Electrochem. Sci. 11 (2016) 4120–4135, https://doi.org/10.1016/s1452-3981(23)17464-5.

[71] K.M. Batoo, Structural and electrical properties of Cu doped $NiFe_2O_4$ nanoparticles prepared through modified citrate gel method, J. Phys. Chem. Solid. 72 (2011) 1400–1407, https://doi.org/10.1016/j.jpcs.2011.08.005.

[72] M. Hashim, S.E. Alimuddin, S. Shirsath, R. Kumar, A.S. Kumar, J. Roy, R.K. Shah, Kotnala, "Preparation and characterization chemistry of nano-crystalline Ni-Cu-Zn ferrite", J. Alloys Compd. 549 (2013) 348–357, https://doi.org/10.1016/j.jallcom.2012.08.039.

[73] K.M. Batoo, M.S. Abd El-Sadek, Electrical and magnetic transport properties of Ni-Cu-Mg ferrite nanoparticles prepared by sol-gel method, J. Alloys Compd. 566 (2013) 112–119, https://doi.org/10.1016/j.jallcom.2013.02.129.

[74] C.M. Kanamadi, J.S. Kim, H.K. Yang, B.K. Moon, B.C. Choi, J.H. Jeong, Magnetoelectric effect and complex impedance analysis of (x)$CoFe_2O_4$+(1-x) $Ba_{0.8}Sr_{0.2}TiO_3$ multiferroics, J. Alloys Compd. 481 (2009) 781–785, https://doi.org/10.1016/j.jallcom.2009.03.085.

[75] Atta ur Rahman, M.A. Rafiq, S. Karim, K. Maaz, M. Siddique, M.M. Hasan, Semiconductor to metallic transition and polaron conduction in nanostructured cobalt ferrite, J. Phys. D Appl. Phys. 44 (2011), 165404, https://doi.org/10.1088/0022-3727/44/16/165404.

[76] E. Barsoukov, J.R. DonaldMac, Impedance Spectroscopy Experiments and Applications, second ed., Wiley, Hoboken, NJ, 2005 https://doi.org/10.1021/ja059742o.

[77] Nesrine Mechi, Abdulrahman Mallah, Sobhi Hcini, Mohamed Lamjed Bouazizi, Effects of sintering temperature on microstructural, magnetic, and impedance spectroscopic properties of $Ni_{0.4}Cd_{0.3}Zn_{0.3}Fe_2O_4$ ferrites, J. Supercond. Nov. Magnetism 33 (2020) 1547–1557, https://doi.org/10.1007/s10948-019-05416-x.

[78] K.M. Batoo, Study of dielectric and impedance properties of Mn ferrites, Phys. B Condens. Matter 406 (2011) 382–387, https://doi.org/10.1016/j.physb.2010.10.075.

[79] M.K. Anupama, B. Rudraswamy, N. Dhananjaya, Investigation on impedance response and dielectric relaxation of Ni-Zn ferrites prepared by self-combustion technique, J. Alloys Compd. 706 (2017) 554–561, https://doi.org/10.1016/j.jallcom.2017.02.241.

[80] M. Chebaane, N. Talbi, A. Dhahri, M. Oumezzine, K. Khirouni, Structural and impedance spectroscopy properties of $La_{0.8}Ba_{0.1}Ca_{0.1}Mn_{1-x}Ru_xO_3$ perovskites, J. Magn. Magn Mater. 426 (2017) 646–653, https://doi.org/10.1016/j.jmmm.2016.10.153.

[81] Hongmei Ren, Pengfei Liang, Zupei Yang, Processing, Dielectric properties and impedance characteristics of $Na_{0.5}Bi_{0.5}Cu_3Ti_4O_{12}$ ceramics", Mater. Res. Bull. 45 (2010) 1608–1613, https://doi.org/10.1016/j.materresbull.2010.07.018.

[82] Fakher Hcini, Sobhi Hcini, Bandar Alzahrani, Efects of sintering temperature on structural, infrared, magnetic and electrical properties of $Cd_{0.5}Zn_{0.5}FeCrO_4$ ferrites prepared by sol-gel route, J. Mater. Sci. Mater. Electron. 31 (2020) 14986–14997, https://doi.org/10.1007/s10854-020-04061-8.

[83] E. Pervaiz, I.H. Gul, Influence of rare earth (Gd^{3+}) on structural, gigahertz dielectric and magnetic studies of cobalt ferrite, J. Phys. Conf. Ser. 439 (2013), 12015, https://doi.org/10.1088/1742-6596/439/1/012015.

[84] K.C. Verma, Navdeep Goyal, Manpreet Singh, Mukhwinder Singh, R.K. Kotnala, Hematite α-Fe_2O_3 induced magnetic and electrical behavior of $NiFe_2O_4$ and $CoFe_2O_4$ ferrite nanoparticles, Results Phys. 13 (2019), 102212, https://doi.org/10.1016/j.rinp.2019.102212.

[85] M. Belal Hossen, A.K.M. Akther Hossain, Influence of Al^{3+} substitution on impedance spectroscopy studies of $Ni_{0.27}Cu_{0.10}Zn_{0.63}Al_xFe_{2-x}O_4$, Adv. Mater. Lett. 6 (2015) 810–815, https://doi.org/10.5185/amlett.2015.5854.

[86] Mithun Kumar Das, M.A. Zubair, Hidekazu Tanaka, A.K.M. Akther Hossain, Study of impedance and magnetoelectric property of lead-free xLCNZFO+(1-x) BGTDO multiferroic composites, Mater. Chem. Phys. 255 (2020), 123575, https://doi.org/10.1016/j.matchemphys.2020.123575.

[87] M.D. Rahaman, T. Nusrat, R. Maleque, A.K.M. Akther Hossain, Investigation of structural, morphological and electromagnetic properties of $Mg_{0.25}Mn_{0.25}Zn_{0.5-x}Sr_xFe_2O_4$ ferrites, J. Magn. Magn Mater. 451 (2018) 391–406, https://doi.org/10.1016/j.jmmm.2017.11.066.

[88] L. Chauhan, N. Singh, A. Dhar, H. Kumar, S. Kumar, K. Sreenivas, Structural and electrical properties of Dy^{3+} substituted $NiFe_2O_4$ ceramics prepared from powders derived by combustion method, Ceram. Int. 43 (2017) 8378–8390, https://doi.org/10.1016/j.ceramint.2017.03.181.

[89] A.K. Pradhan, T.K. Nath, S. Saha, Impedance spectroscopy and electric modulus behavior of molybdenum doped cobalt-zinc ferrite, Mater. Res. Express 4 (2017), 076107, https://doi.org/10.1088/2053-1591/aa7c8c.

[90] J.R. Macdonald, Scaling and modeling in the analysis of dispersive relaxation of ionic materials, J. Appl. Phys. 90 (2001) 153–161, https://doi.org/10.1063/1.1374480.

[91] S. Pattanayak, B.N. Parida, P.R. Das, R.N.P. Choudhary, Impedance spectroscopy of Gd doped $BiFeO_3$ multiferroics, Appl. Phys. A 112 (2013) 387–395, https://doi.org/10.1007/s00339-012-7412-6.

[92] S.G. Kakade, Y.R. Ma, R.S. Devan, Y.D. Kolekar, C.V. Ramana, Dielectric, complex impedance, and electrical transport properties of erbium (Er^{3+}) ion-substituted nanocrystalline, cobalt-rich ferrite ($Co_{1.1}Fe_{1.9-x}Er_xO_4$), J. Phys. Chem. C 120 (2016) 5682–5693, https://doi.org/10.1021/acs.jpcc.5b11188.

[93] A. Manzoor, M.A. Khan, M. Shahid, M.F. Warsi, Investigation of structural, dielectric and magnetic properties of Ho substituted nanostructured lithium ferrites synthesized via auto-citric combustion route, J. Alloy Compd. 710 (2017) 547–556, https://doi.org/10.1016/j.jallcom.2017.03.154.

[94] M.N. Akhtar, M.A. Khan, M.R. Raza, M. Ahmad, G. Murtaza, R. Raza, S.F. Shaukat, M.H. Asif, M. Saleem, M.S. Nazir, Structural, morphological, dielectric and magnetic characterizations of $Ni_{0.6}Cu_{0.2}Zn_{0.2}Fe_2O_4$ nanocomposites for multilayer chip inductor (MLCI) applications", Ceram. Int. 40 (2014) 15821–15829, https://doi.org/10.1016/j.ceramint.2014.07.109.

[95] Mithun Kumar Das, M.A. Zubair, Hidekazu Tanaka, A.K.M. Akther Hossaina, An experimental insight of the multiferroic properties of magnetoelectrically coupled xLNCZFO+(1-x)BSTDO composites, J. Magn. Magn Mater. 502 (2020), 166449, https://doi.org/10.1016/j.jmmm.2020.166449.

[96] M.J. Miah, M.N.I. Khan, A.K.M. Akther Hossain, Weak ferromagnetism and magnetoelectric effect in multiferroic x$Ba_{0.95}Sr_{0.05}TiO_3$+ (1-x)$BiFe_{0.9}Gd_{0.1}O_3$ relaxors, J. Magn. Magn Mater. 401 (2016) 600–611, https://doi.org/10.1016/j.jmmm.2015.10.083.